JOURNAL OF MATERIALS SCIENCE 24 (1989) 1429–1438

Material variability in composition and structure of a Type 316 stainless steel submerged arc weld metal

G. PIATTI, M. VEDANI
Materials Science Division, Joint Research Centre – Ispra Establishment, Commission of the European Communities, 21020 Ispra (Va), Italy

Type 316 austenitic stainless steel submerged arc weld (SAW) deposited metal, produced by joining two heavy (50 mm) thickness plates with a multipass procedure and using Type 316L filler metal, was characterized from both a compositional and structural point of view (optical and scanning electron microscopy observation, energy-dispersive X-ray elemental analysis and ferrite content and hardness measurements). Important features such as columnar grain macrostructure, mainly cellular-dendritic and a duplex (γ-austenite matrix plus δ-ferrite second phase) microstructure were observed according to the occurrence of a ferritic-austenitic weld-pool solidification mode followed by a solid-state $\delta \rightarrow \gamma$ transformation. The weld deposited metal was characterized along the thickness by significant variations in composition and ferrite morphology, distribution and content because of the influence of the filler metal chemistry and the thermal cycles experienced by each pass during subsequent passes.

1. Introduction

The characteristics of fusion welds, related to service conditions such as mechanical behaviour and corrosion resistance, are strongly influenced by the morphology and the segregation patterns occurring during the weld pool solidification process [1–3]. A detailed knowledge of the solidification structure in the deposited metal of the fusion welds is, therefore, important for the possible implications in the design and monitoring of welded components, especially those to be used in future nuclear installations such as fast reactors [4–6] or thermonuclear fusion devices [7] which require extremely high safety standards. Type 316 austenitic stainless steel appears to be the likely candidate material for these components [6, 7].

From previous work concerning the characterization of Type 316 stainless steel welds, it can be seen that there are significant differences in composition and microstructure between various regions within the weld deposited metal. There are variations in dislocation density, substructure size, grain diameter, content, distribution and morphology of δ-ferrite and other phases such as carbides and sigma-particles which might be present and, last but not least, chemistry (composition adjustment by filler metal) [8–15]. There is concern that these changes generally cause losses in ductility properties. Specifically, a considerable heterogeneity is to be expected in the case of thick (greater than 25 mm) submerged arc-weld (multipass procedure) deposited Type 316 stainless steel because of the high energy input involved in this process (higher than that found in other welding processes) [16] and of the complex thermal cycling experienced by each pass during deposition of the subsequent passes during the welding [8, 15]. The fundamental role of δ-ferrite in the prevention of solidification cracking, as should be noticed [17–21], has been shown.

In the present work the authors have compositionally and structurally characterized a thick (50 mm) Type 316 SAW deposited metal by optical and scanning electron microscopy, energy-dispersive X-ray analysis and ferrite content and hardness measurements. The goal of the research was to assess the material variability in the weld metal of a heavy section Type 316 weld.

2. Materials and experimental conditions

The material used was a 50 mm thick Type 316 stainless steel plate (Uddeholm heat LK 4290) supplied in solution annealed conditions. This heat has been thoroughly investigated [22–25]. The chemical analysis (wt %) is given in Table I. The compositions listed are in accordance with a restricted specification, proposed by Wood for Type 316, to be used in liquid metal fast breeder reactors [6] and characterized by a high nitrogen level, a relatively low carbon level and some restrictions in trace elements which are intended to increase tensile and creep properties and improve weldability. The microstrucure proved to be fully austenitic with a mean grain size of about 90 μm [25]. Non-metallic inclusions (alumina and globular oxides) and no carbide precipitates were observed.

The weld was realized by Zanon (Schio-Italy) with an automatic SAW process by joining two sections cut from the plate along the longest (1260 mm) side. The joint configuration a symmetrical double-U groove is shown in Fig. 1a and the sequence of build-up

0022–2461/89 $03.00 + .12

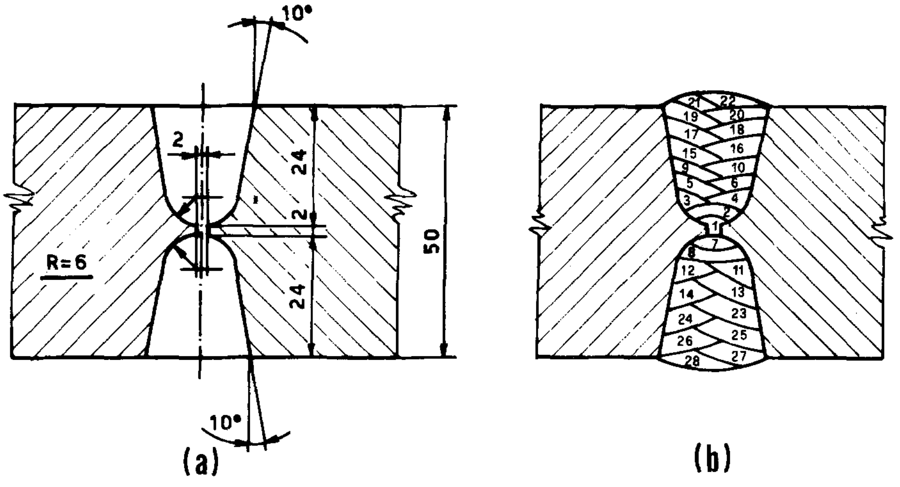

Figure 1 Details of the submerged arc-welding with multipass procedure. (a) shape and dimensions (mm) of the symmetrical double-U groove profile; (b) sequence of the weld passes.

operations (28 passes) is illustrated in Fig. 1b. Two Type 316L commercial filler metals were used. Their compositions (Table I) were chosen with respect to the base metal (reduction of nickel content with a simultaneous increase in chromium) in order to produce between 3 and 8% of δ-ferrite in the weld deposit as requested by established practice in welding to prevent hot cracking [13]. Further and more detailed information on the welding conditions employed is listed in Table II. The welded joint was checked by non-destructive techniques (fluorescent penetrant liquid method and X-ray radiography). An excellent weld soundness was found.

Some transverse sections of the weld were cut and prepared by mechanical polishing and electrolytical etching (10% oxalic acid or 50% HNO_3 solution) for observation with an optical microscope (Leitz MM6) and a scanning electron microscope (Philips 505) and for line scans and quantitative microchemical analysis by energy-dispersive X-ray elemental detection (ORTEC system 5000). Other sections were prepared only by mechanical polishing for evaluation, along the weld thickness, of the profile of the ferrite (volume) content using a permeability meter (Fisher ferritescope) and for measurement of the Vickers hardness in various zones of the weld by a Leitz indentation tester (10 kg load).

3. Results and discussion

3.1. Weld appearance

A macroetched view of a cross-section of the investigated weld is shown in Fig. 2. The weld appearance is characterized by good wetting, sidewall fusion and liquid penetration, by build-up of the successively overlaid weld beads reflecting the multipass procedure and by a characteristic macrostructure oriented along the grains (columnar). These features mean that the moving pool of molten metal, produced by the SAW process, could solidify within the joint by epitaxial growth from crystals favourably oriented at the initial solid–liquid interface and from bead to bead through a competitive process between the adjacent columnar grains [1, 2, 26]. This competitive growth was controlled by the weld pool geometry which, as seen on the weld surface (Fig. 3), was of the "tear-shaped" type [2, 3]. Unfortunately, in this type of pool geometry, preferred orientations can develop during solidification with the final effect of a resulting anisotropy in weld properties [3].

The solidification substructure of the weld was found to be mainly cellular or cellular-dendritic. Narrow zones of planar growth were, however, found along the fusion line. Moreover, no equiaxed grains were found. These features are shown in Fig. 4. The transition from planar to cellular substructure can be

TABLE I Chemical composition (wt %) of materials tested

Material	Cr	Ni	Mo	C	N	Si	Mn	P	S	Ti	Nb	Cu	Fe
AISI 316 as-received solution annealed (50 mm thick) plate	16.9	12.3	2.48	0.052	0.082	0.34	1.67	0.020	0.009	0.006	0.008	0.007	rest
AISI 316L filler metal A (for the first pass)	18.65	12.25	2.82	0.020	–*	0.98	0.79	–	–	–	–	–	rest
AISI 316L filler metal B (for the passes 2-28)	18.15	10.80	2.65	0.016	–*	0.42	1.39	0.011	0.011	–	–	–	rest
Weld metal													
Root deposit	17.80	11.75	2.49	0.03	0.07	0.48	1.52	0.031	0.027	0.003	0.012	0.005	rest
Front pass deposit	17.33	11.24	2.54	0.03	0.07	0.67	0.99	0.037	0.029	0.003	0.009	0.092	rest
Back pass deposit	17.24	11.08	2.63	0.03	0.07	0.65	0.97	0.035	0.028	0.003	0.009	0.125	rest

*For the equivalent calculation a nitrogen content of 0.04 was used when the analysis was not available.

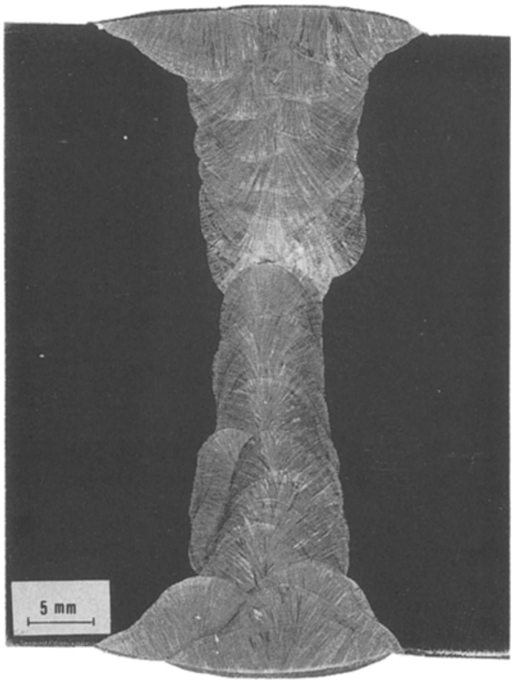

Figure 2 Macrograph of an (etched) cross-section of the Type 316 weld showing as-deposited weld metal geometry and solidification macrostructure.

TABLE II Welding parameters

Process	Submerged-arc welding*
Joint design	Double-U-groove
Number of passes	28
Interpass temperature	55° C (max)
Post heat	None
Electrode wire	2.4 and 3.25 mm-dia.
Flux	Neutral
Current	280 to 340 A
Voltage	30 V
Travel speed	45 to 58 cm min^{-1}
Heat input rate	1.05 to 1.12 MJ m^{-1}

*First pass made by shielded metal-arc welding

understood in terms of the ratio G/R [27] where G is the thermal gradient in the liquid and R the solidification rate. At high ratio values there is the prevalence of planar growth whereas when the ratio decreases there is a breakdown into cellular or cellular-dendritic growth modes. The decrease in the G/R ratio values was, however, not sufficient to produce equiaxed dendritic growth, even in the region of the centreline of the pool where G shows the lowest and R the highest values.

3.2. Solidification mode and ferrite morphology

A variety of duplex (γ-austenite plus δ-ferrite second phase) microstructures were observed by optical microscopy in the investigated as-deposited held (as was expected from the literature on austenitic stainless steel welds [26, 28–36]) paying particular attention to morphology and δ-ferrite location (inter or intragranular) which is recognized as being difficult to determine [33]. The observations by optical microscopy (summarized in the selected pictures of Fig. 5) and also by SEM allowed us to assess the solidification mode according to the Suutala Takalo and Moisio solidification model in austenitic stainless steel welds [30], which refers to three types of microstructures called A, B and C, respectively. In our case two types of microstructures were found.

(i) Type A: a small amount of weld (about 10%) solidified with a resulting structure (Figs 5a and b) characterized by a distribution of δ-ferrite in vermicular form at the cell boundaries and of austenite between the cells. An austenitic-ferritic (AF) solidification mode (often termed primary austenite solidification [36]) occurred: the austenite is the primary solidifying or leading phase and δ-ferrite solidifies from the rest of the melt [30, 33].

(ii) Type B: most of the weld (about 90%) solidified with a final morphology characterized by vermicular ferrite (Figs 5c and d) located at the cell axes and lathy ferrite (Figs 5e and f). In this case it is a matter of ferritic-austenitic (FA) solidification mode (often termed primary ferrite solidification [36]): the leading phase is the δ-ferrite and austenite solidifies from the rest of the melt and also through a solid-state $\delta \rightarrow \gamma$ transformation occurring at high temperature [30, 33].

The solidification mode FA assessed above on the basis of phenomenological observations, has also been

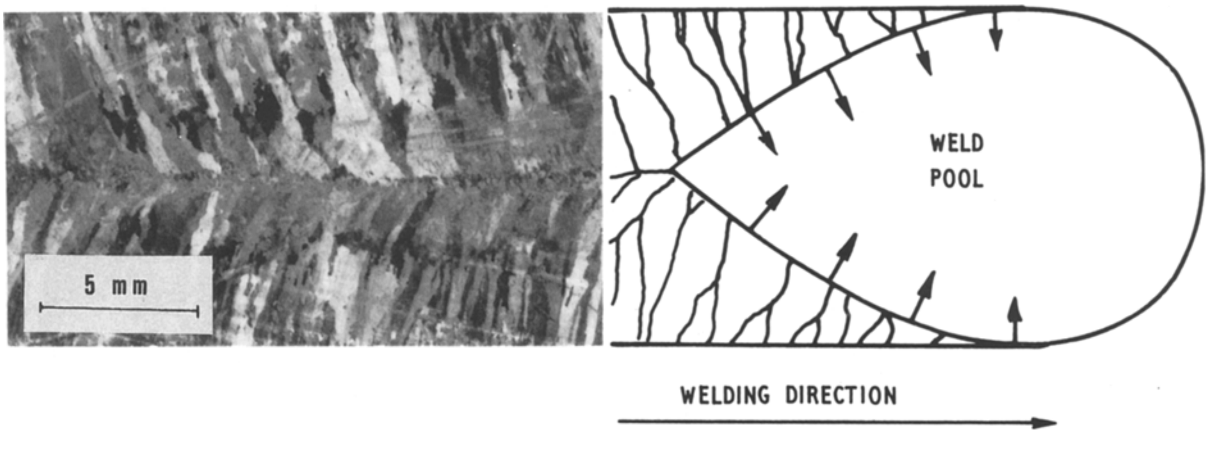

Figure 3 View of the (etched) weld surface showing columnar development typical of a tear-drop shaped weld pool (schematic representation) with the cell growing perpendicular to the fusion line in the plane of the sheet [2, 3].

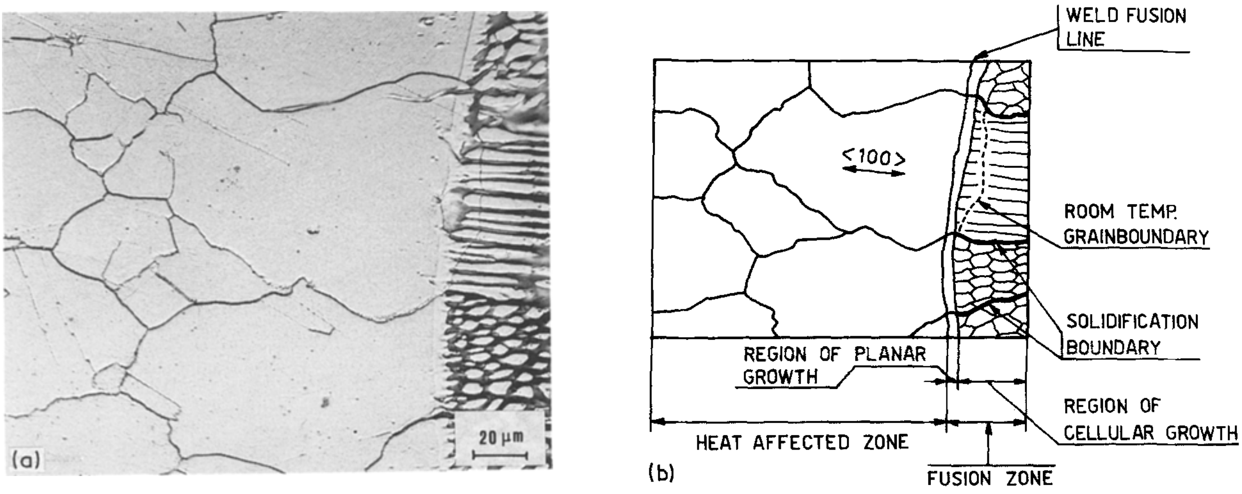

Figure 4 Example of epitaxial growth of the cell from the favourably oriented grains of the unmelted metal; (a) micrograph; (b) idealized schematic representation (⟨1 0 0⟩ is the preferred crystallographic growth directions in fcc metals).

predicted in terms of chromium and nickel equivalents according to the formulae proposed by Hammar and Svensson [37] which give, for the conventional welds of AISI Type 300 steel series, a better correlation between chemistry and solidification mode than De Long–Schaeffler equivalents [38], as reported in the literature [33, 39]. Table III shows, in fact, for the various weld metal regions (and also for the base metal and filler metals) the values of the above equivalents and their ratios calculated from the chemical compositions, respectively (listed in Table I), and the corresponding solidification modes predicted according to plots of the above-mentioned chromium and nickel equivalent values in the Hammar–Svensson

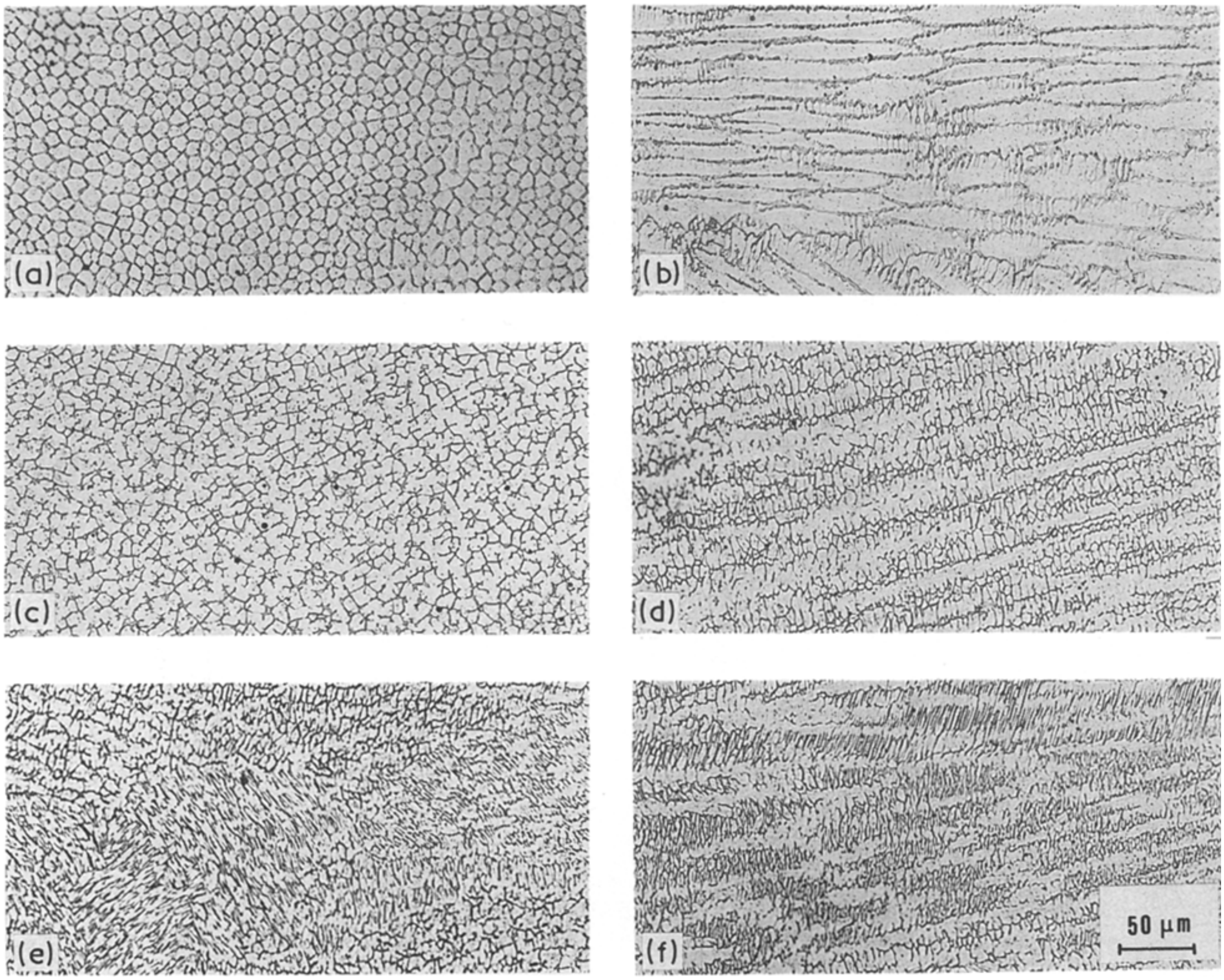

Figure 5 Typical microstructures observed in weld-deposited metal. (a and b) vermicular δ-ferrite located at the cell-boundaries (austenitic-ferritic solidification mode); (c and d) vermicular δ-ferrite located at the cell axes (ferritic-austenitic solidification mode); (e and f) lathy σ-ferritic (ferritic-austenitic solidification mode). The micrographs (a), (c), (e) and (b), (d), (f) correspond to the sectioning position normally and parallel to columnar grains, respectively.

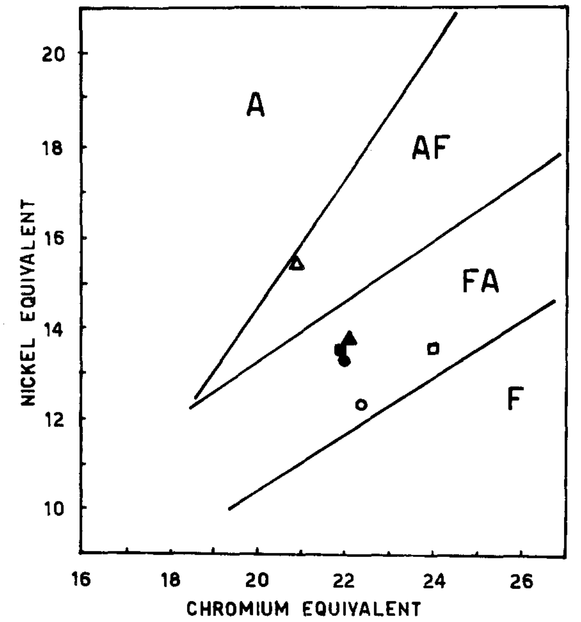

Figure 6 Relationship between the composition and solidification mode in terms of Hammar–Svensson equivalents (△ base metal, □ filler metal A, ○ filler metal B, ▲ root deposit, ■ front passes deposit, ● back passes deposit).

diagram [37] and their location relative to solidification fields (Fig. 6). There is evidence of an excellent correlation between the FA solidification mode predicted for the root, front pass and back pass deposits (Table III) and the FA mode previously observed for 90% of the weld deposit. The solidification mode AF observed for the remaining 10% of the weld observed in some areas near to the HAZ–weld deposit interface can be easily explained in terms of a stronger dilution from the base metal which presents the AF solidification mode (Tables III) but is very near to the A solidification field (Fig. 6). On the contrary, as expected, the solidification modes of filler metals (Table III) is FA but close to the F solidification field (Fig. 6).

Typical EDS spectra from γ-austenite matrix and δ-ferrite second phase are presented in Fig. 7. A comparison of the relative peak heights of chromium and iron and of nickel and iron shows that the chromium content is higher in ferrite and the nickel content is higher in austenite. This trend in relative composition was confirmed by the qualitative compositional profiles determined for the chromium and nickel elements within the weld in the root region following scan lines crossing particles of δ-ferrite. Examples are given in Fig. 8. Both profiles correspond to areas characterized by a ferritic austenitic solidification mode. There is clear evidence that the austenite (matrix) is richer in nickel and poorer in chromium whereas the δ-ferrite phases are richer in chromium and poorer in nickel. In terms of actual composition some EDS data are reported in Table IV (considering only the principal alloying elements chromium, nickel and molybdenum). The reported values were measured for the root deposition (analysed zones 1 and 2) in the numbered points of the micrograph of Fig. 9. The results of Table IV confirm the results of Figs 7 and 8 quantitatively, and are in satisfactory agreement with segregation literature data on FA welded structures of austenitic stainless steels [13, 19, 20, 26, 31, 33–36, 40]. There is then a confirmation of segregation effects due to alloy partitioning and microsegregation during solidification and solid-state $\delta \rightarrow \gamma$ transformation. The lack of data does not, however, permit a discrimination between the influence of solidification and that of solid state transformation and also between alloy partitioning and microsegregation. Table IV indicates that the segregation effects are, however, more elevated for the front pass deposit (analysed zone 3). This means that the decomposition of δ-ferrite takes place for the latter deposit at lower temperatures than for the former.

Quantitative EDS analyses showed no evidence of carbides and σ-phase formation. Carbides were not expected because of the low carbon content on the weld deposit, 0.03% (Table I), because of the use of filler metals with low carbon content, 0.016 and 0.020% (Table I). On the other hand, the σ-phase could appear in the weld deposit because in the austenitic stainless steel multirun welds there are areas exposed during thermal cycles in the course of welding to temperatures in the range 500 to 900° C in which σ-phase formation could occur [41]. Evidently, in the case of the present welding the dwell time at these temperatures did not reach the minimum time for the beginning of the transformation of δ-ferrite into the σ-phase which is of the order of 30 to 40 sec. [41].

3.3. Ferrite content

The occurrence of the vermicular or lathy morphology is related not only to the solidification mode as discussed above, but also to the ferrite content. The

TABLE III Chromium and nickel equivalent values for the ferrite content and solidification mode

	De Long equivalents*			Hammer and Svensson equivalents†			
	Cr_{eq}	Ni_{eq}	Ferrite content (vol %)	Cr_{eq}	Ni_{eq}	Cr_{eq}/Ni_{eq}	Solidification mode
Base metal	19.89	17.16	0	20.84	15.22	1.37	AF
Filler metal A	22.94	14.44	10.5	23.98	13.50	1.78	FA
Filler metal B	21.43	13.18	11.5	22.41	12.15	1.84	FA
Root deposit	21.03	15.51	3.5	21.98	13.88	1.58	FA
Front passes deposit	20.92	14.74	5.0	21.86	13.29	1.64	FA
Back passes deposit	20.86	14.54	6.0	21.85	13.16	1.66	FA

*De Long equivalents [38] $Cr_{eq} = \%Cr + \%Mo + 1.5\%Si + 0.5\%Nb$ $Ni_{eq} = Ni + 0.5\%Mn + 30\%C + 30\%N$

†Hammar and Svensson equivalents [37] $Cr_{eq} = \%Cr + 1.37\%Mo + 1.5\%Si + 2\%Nb + 3\%Ti$ $Ni_{eq} = \%Ni + 1.31\%Mn + 22\%C + 14.2\%N + \%Cu$

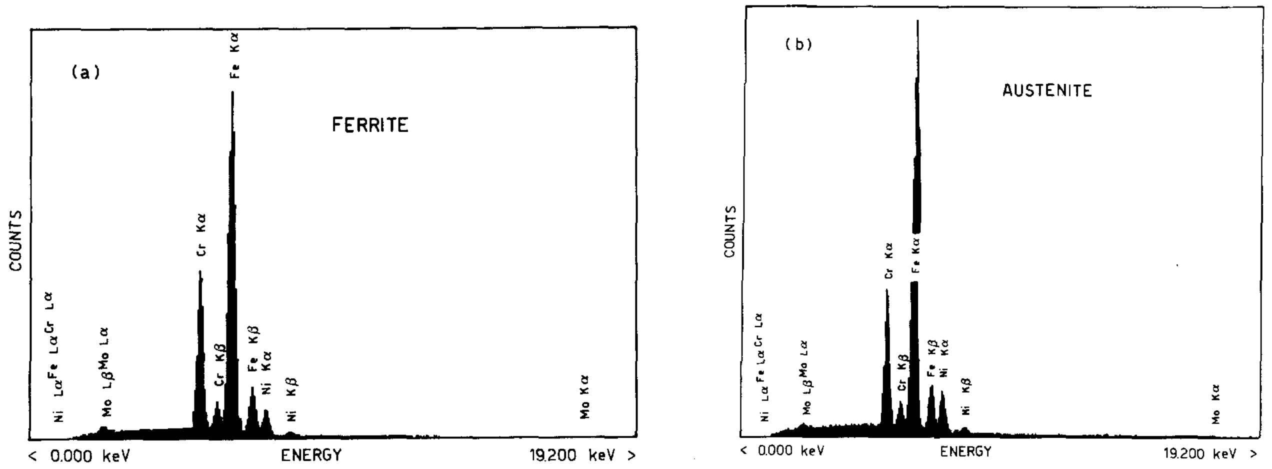

Figure 7 Typical EDS spectra found in Type 316 stainless steel weld-deposit. (a) ferrite; (b) austenite.

ferrite volume fractions measured along the thickness in a transverse section of the present weld are reported in Fig. 10. There is clear evidence of a ferrite value decrease from weld surface to the weld centre and a minimum value of 3.9% is found on a point where the beads from opposite (front and back passes) regions impinge (see Fig. 2). By comparing the observed ferrite morphologies with corresponding measured ferrite values it can be seen that the ferrite is vermicular when the content is low (approximately ⩽6%), is lathy when the content is high (approximately ⩾12%), whereas at intermediate ferrite contents from 6 to 12, both vermicular and lathy are present (this is the case for most of the areas in the weld deposit). These observations are in excellent agreement with results from previous literature [29] on the influence of ferrite content on its morphology in some austenitic weld metals.

The ferrite content can be also predicted in terms of the De Long–Schaeffler equivalents and corresponding diagram [38] which relate the alloy chemistry to the volume fraction of ferrite present in austenitic steels. The values of chromium and nickel equivalents, calculated for different regions of present weld-deposit on the basis of their chemical analyses (Fig. 1), respectively, are given in Table III together with corresponding ferrite content predicted from the De Long–Schaeffler diagram (Fig. 11). There is good agreement between the measured ferrite contents (Fig. 10) and the predicted values (Fig. 11) confirming the validity of the De Long–Schaeffler diagram [38].

It should be observed that in Fig. 11 the points representing the front passes and the back passes are located along the line connecting the base metal and the filler metal B as expected, because one is dealing with deposits produced by the use of the filler metal B alone, whereas the point representing the root pass deposit is located on a line intermediate between the line connecting the base metal and the filler metal A and the line connecting the base metal and the filler metal B, because this deposit is produced with the use of both filler metals. Moreover, from Fig. 11 it is possible to determine the dilution, which is generally expressed as the percentage of the base metal in the final weld, according to a simple rule [42]. The levels of dilution are for the root pass, front pass and back pass deposits: 51, 43 and 37%, respectively. This means that the dilution from parent metal is more important in the root deposit than in the front and back deposits because of the lesser volume in the root region. In fact, joint configuration is a major factor in controlling dilution although it also depends on the procedure variables [42].

Dilution has a great influence on the ferrite content

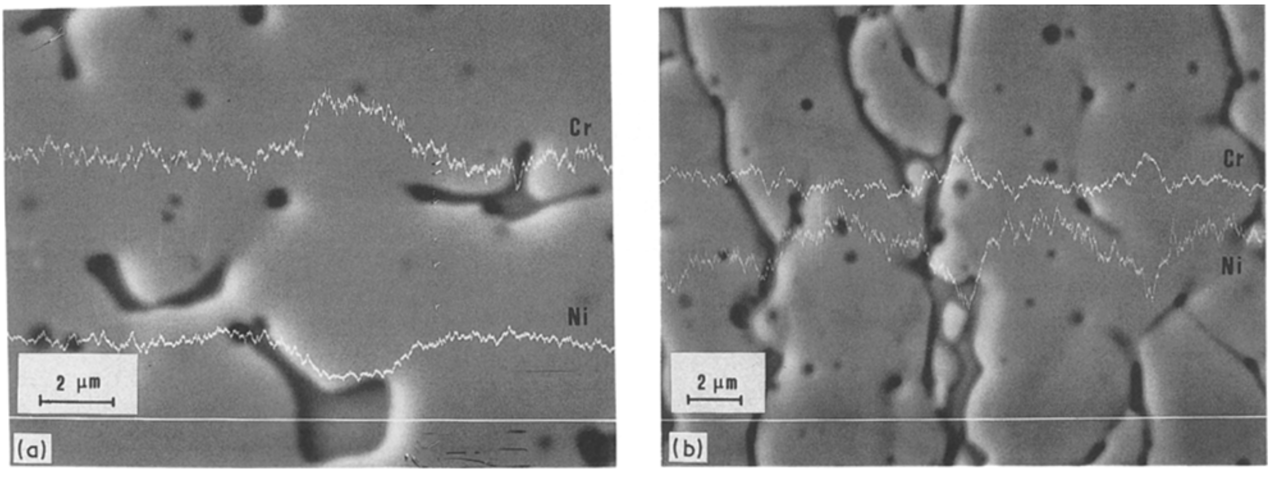

Figure 8 Line scans across sections. (a) normal; (b) parallel to columnar grains, performed on an area located in the root region.

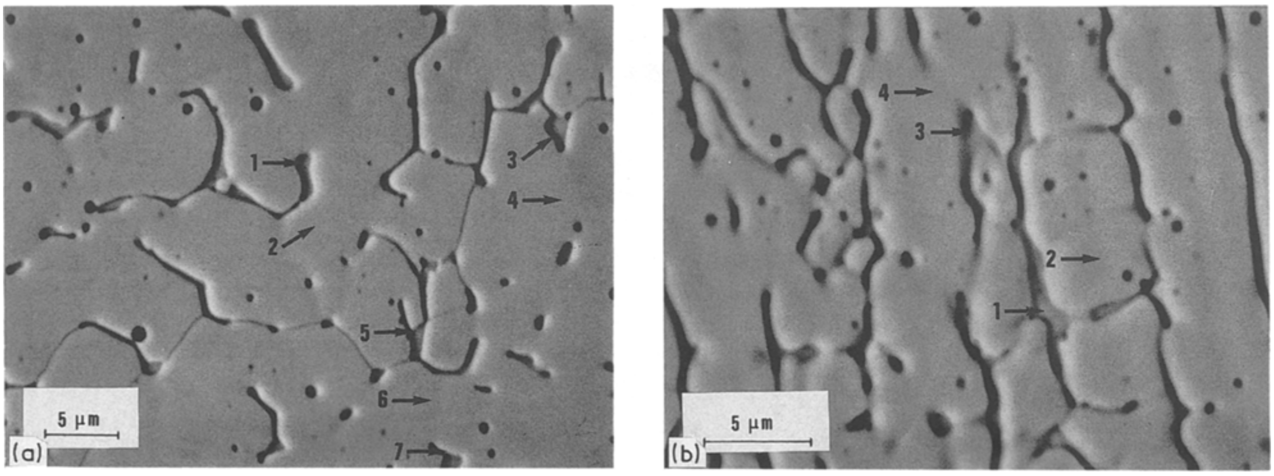

Figure 9 Location of the numbered points whose corresponding EDS analyses are reported in Table IV. (a) area 1; (b) area 2.

of welds. In the present weld it explains in part the lower content of the ferrite volume fraction measured in the root region with respect to other regions of the weld (Fig. 10). Dilution decreases the ferrite content when the chemistry of the base metal has a lower calculated ferrite potential (based on the De Long–Schaeffler diagram) than that of the undiluted metal [42]. Ferrite contents indicated in Table III show this situation. In fact, the base metal has a virtually zero ferrite fraction and filler metals A and B have 10.5 and 11.5%.

The variation in ferrite content of Fig. 10, however, depends also on ferrite dissolution resulting from thermal cycles during subsequent weld passes, which is more important in root pass, as was observed previously by other authors [15, 32]. In the present case the above behaviour can be explained in more detail by considering the Fe–Cr–Ni pseudo-binary diagram illustrated in Fig. 12, which can be considered as representative of the phase equilibrium and of the sequence of phase separation in our weld deposit.

TABLE IV Energy dispersive X-ray analysis in weld metal.

Analysed zone		Cr	Ni	Mo	Fe	Phase
1 Root deposit	1	20.98	8.41	2.13	66.48	Phase
	2	18.20	12.44	2.03	65.33	Matrix
	3	22.20	7.25	2.15	66.40	Phase
	4	18.24	11.93	2.20	65.62	Matrix
	5	20.14	9.11	2.22	66.53	Phase
	6	18.89	10.47	2.20	66.44	Matrix
	7	21.64	8.08	2.58	65.71	Phase
2 Root deposit	1	20.02	8.64	2.71	66.63	Phase
	2	17.67	12.23	2.94	65.16	Matrix
	3	18.50	10.65	2.18	66.68	Phase
	4	17.90	12.49	2.98	64.63	Matrix
3 Front passes deposit	1	23.52	6.13	4.84	63.70	Phase
	2	18.79	11.96	2.84	64.37	Matrix
	3	23.26	6.23	7.04	61.45	Phase
	4	18.88	10.47	2.33	66.85	Matrix
	5	19.76	9.79	3.20	65.06	Matrix
	6	18.51	11.99	2.79	65.19	Matrix
	7	18.56	11.35	2.67	65.69	Matrix
	8	23.22	5.56	4.72	64.78	Phase
	9	18.80	11.70	4.10	62.40	Phase
	10	18.00	12.60	3.60	62.80	Matrix

It is a vertical section through the Fe–Ni–Cr phase diagram at 64 wt % Fe which represents approximately the weld composition of Tables I and III. The (Cr/Ni) equivalent ratios of 1.58 corresponding to root deposit and 1.65 representing both front and back pass deposits, place the compositions to slightly chromium-rich sides of the eutectic valley, the composition C_2 (front and back pass deposits) being nearer to the σ-field than C_1 (root pass deposit). From some measurements on complex thermal cycles of multirun welding in 18-8 stainless steel (heat input and interpass temperature conditions similar to present weld) [45] at a maximum temperature of 1200° C in a weld bead during the deposition of a subsequent bead, it is obvious that:

(a) in the case of the root deposit (composition C_1) as the metal is reheated to 1200° C (a temperature below the γ-solvus temperature 1275° C), the residual ferrite should transform to austenite;

(b) in the case of the front and back pass deposit (composition C_2) as the metal is reheated to 1200° C (a temperature above the δ-solvus temperature 1065° C), the residual ferrite should transform to austenite up to the cited δ-solvus temperature but reform above it. Upon cooling, obviously, reprecipitated ferrite may transform back to austenite.

As a result, in the first case, the ferrite dissolution is permanent (no reformed δ) and the dissolution rate is higher because the temperatures are higher and the diffusion rate increases with temperature. The ferrite content temperature change effects because of a thermal cycling contributes then to a lowering of the ferrite value in the root deposit (Fig. 10).

3.4. Microstructure

The observed networks of cells and of (vermicular of lathy) δ-ferrite are contained in grains whose average size quantitatively estimated by a random line-intercept method was of the order of 90 μm, a value comparable to that of the base metal [25]. It should be noticed that the location of the room temperature grain boundary is different from that of the (columnar) solidification grain boundary, as shown in Fig. 4. In fact, during the weld metal cooling following solidification, the original solidification

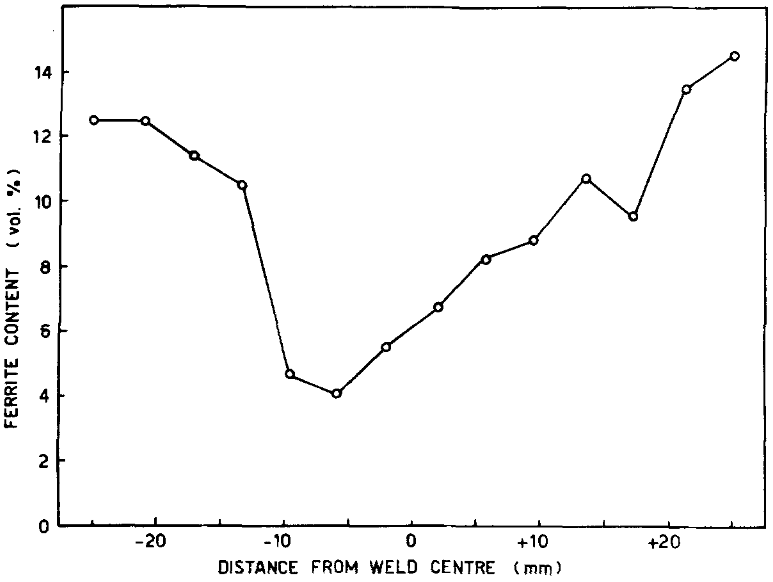

Figure 10 Ferrite content measured along the thickness of the as-deposited weld in a transverse section of the Type 316 stainless steel weld (the negative values of the distance correspond to front pass deposits).

boundary (containing cell patches having the same orientation) migrated, crossing the cells. Similar observations have been made previously by other authors who explain the migration as the effect of plastic strain due to thermal stresses [20].

With regard to the fine microstructure, according to the literature on Fe–Cr–Ni–Mo austenitic steel welds [10, 11], it is a matter of solidification dislocation substructures linking the δ-ferrite into a subgrain structure by accommodating the mismatch between adjacently growing dendrites in the course of the weld pool solidification [11, 12]. The substructure size was roughly estimated to be of the order of $10\,\mu m$ (SEM observations) but there were variations depending upon the position in the weld.

3.5. Hardness

The profiles shown in Fig. 13 revealed that the values found near to the root deposit are higher than those found in the front pass deposit region and near to the weld surface. This trend, as a function of the thickness, can be explained in terms of dislocation hardening (resulting from thermal stresses originating from welding which causes significant deformation on beads) which is higher in the root region, as this experienced more thermal cycles [46]. A gradual decrease of the dislocation density from weld centre to weld surface was experimentally shown in TEM studies previously performed in austenitic stainless steel weld deposits [11]. It should be observed that the maximum values were found in an area a few millimetres above the weld centre where the two opposite (front and back) bead sides impinge (Fig. 2). Room temperature hardness data shown in Fig. 13 can also be considered as a room temperature strength evaluation because of an often observed strict correlation between hardness and yield and ultimate strengths [47].

4. Concluding remarks

The results of the present characterization study of a Type 316 austenitic stainless steel weld deposited

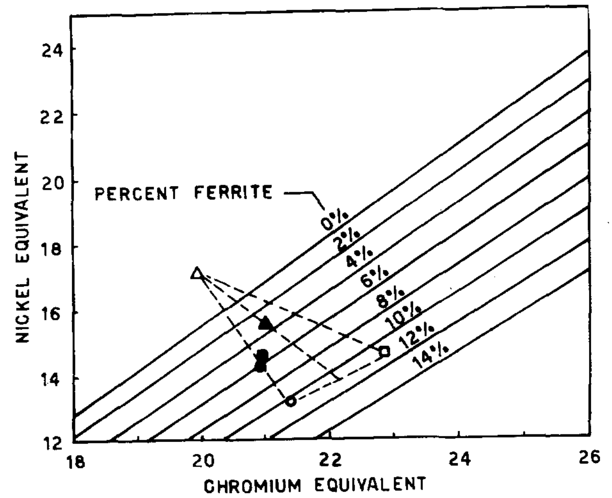

Figure 11 Relationship between the composition and ferrite content in terms of De Long–Schaeffler chromium and nickel equivalents. (△ base metal, □ filler metal A, ○ filler metal B, ▲ root deposit, ■ front passes deposit, ● back passes deposit)

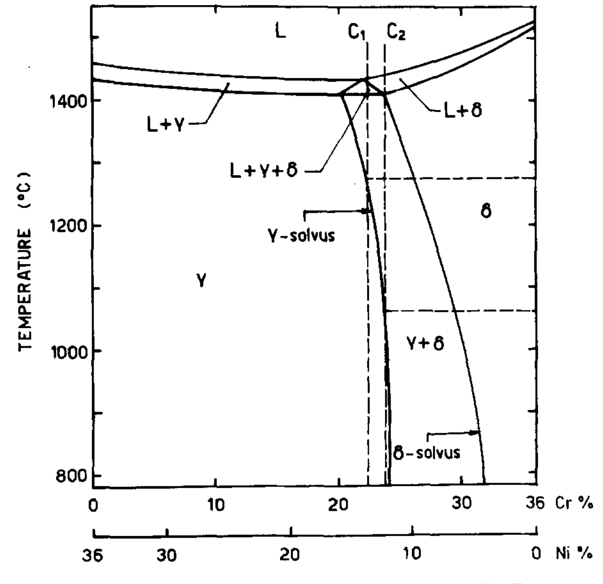

Figure 12 Fe–Cr–Ni pseudo-binary diagram: 64 wt % Fe. It was drawn by the authors from data on liquidus and solidus surfaces [43] and a series of isotherms [44] on the ternary diagram.

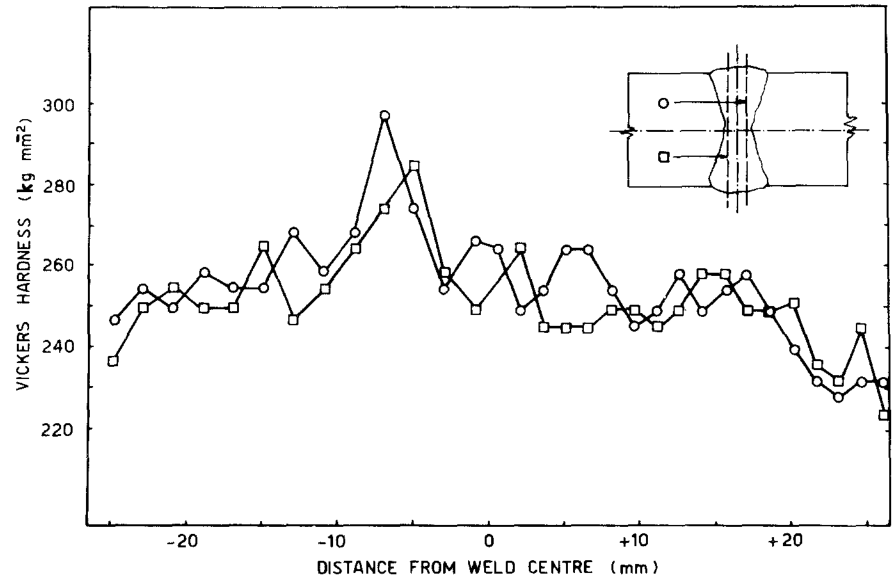

Figure 13 Hardness profiles along the thickness of the as-deposited weld, in a transverse section of the Type 316 stainless steel weld (the negative values of the distance correspond to front pass deposits).

metal, fabricated by joining thick (50 mm) plates with the multipass SAW procedure and using two 316L filler metals, confirm an expected compositional and microstructural variability along the thickness of the weld. Principally, a variation in chemistry has been seen (related to differences in dilution of base metal resulting from weld geometry and to the use of Type 316 filler metals of different compositions), in ferrite content, distribution and morphology (related to chemistry, to solidification mode and to dissolution of ferrite resulting from thermal cycles during subsequent passes), and in hardness (related to dislocation density depending on thermal stresses originated on welding). However, the high number (28) of passes used and the holding of the interpass temperature to below 55° C (Table II) allowed control of the weld composition. In conclusion, the observed material variability is in line with literature data on stainless steel welds.

With regard to the macrostructural variability within the weld, such as differences in columnar grain size, substructure size and morphology (cells and cellular-dendrites) which are related principally to weld pool geometry and welding conditions, these are less relevant than the compositional and microstructural variations mentioned above. They can be equally important, however, with respect to their influence on mechanical behaviour (for instance, the effect of preferred orientation developed during weld solidification on anisotropy in tensile tests). In all cases an evaluation of the weld deposited metal by mechanical testing (tensile testing for example) should allow an additional characterization of the variability of the present weld and research in this sense is planned by the authors on the same Type 316 weld.

Acknowledgements

The authors would like to thank M. Airola and H.A. Weir for their assistance in the experimental work; G. Franzetti for drawing preparation and F. Bo for chemical analyses. Thanks are also due to Dr Ing. G. Verzeletti for supplying the Type 316 stainless steel weld and relative information. EDS analyses were performed by Dr E. Signorelli of ITM-CNR Cinisello (Milano), Italy. Finally, helpful discussions with Professor G. Bernasconi (Politecnico di Milano, Italy) and Dr D. G. Rickerby are gratefully acknowledged.

References

1. W. F. SAVAGE, C. D. LUNDIN and A. H. ARONSON, *Welding J.* **44** (1965) 175-s.
2. W. F. SAVAGE and A. H. ARONSON, *ibid.* **45** (1966) 85-s.
3. G. J. DAVIES and J. G. GARLAND, *Int. Metall. Rev.* **20** (1975) 83.
4. R. T. KING, D. A. CANONICO and C. R. BRINKMAN, *Welding J.* **54** (1975) 265-s.
5. K. H. KLOOS, J. GRANACHER and W. SCHIEBLICH, Report RAP-044D, Commission of the European Communities, Brussels, 1983.
6. D. S. WOOD, in Proceedings of the International Conference on Mechanical Behaviour and Nuclear Applications of Stainless Steels at Elevated Temperatures, Varese (Italy) 1981 (The Metals Society, London, 1982) Book 280, p. 238.
7. G. PIATTI and P. SCHILLER, *J. Nucl. Mater.* **141-143** (1986) 417.
8. A. L. WARD, *Nucl. Technol.* **24** (1974) 201.
9. C. F. ETIENNE, F. ROODE and O. V. ROSSUM, in Proceedings of International Conference on Engineering Aspects of Creep, Sheffield, 1980 (Institute of Mechanical Engineering, London, 1980) Vol. 2, p.113.
10. C. A. P. HORTON, P. MARSHALL and R. G. THOMAS, in Proceedings of International Conference on Mechanical Behaviour and Nuclear Applications of Stainless Steels at Elevated Temperatures, Varese (Italy) 1981 (The Metals Society, London, 1982) Book 280, p. 66.
11. J. R. FOULDS and J. MOTEFF, *Welding J.* **61** (1982) 189-s.
12. J. R. FOULD, J. MOTEFF, V. K. SIKKA and K. W. McENERNEY, *Metall. Trans. A* **14A** (1983) 1357.
13. R. A. FARRAR and R. G. THOMAS, *J. Mater. Sci.* **18** (1983) 3461.
14. R. L. KLUEH and D. P. EDMOND, *Welding J.* **65** (1986) 156-s.
15. I. GOWRISANKAR, A. K. BHADURI, V. SEETHARAMAN, D. D. N. VERMA and D. R. G. ACHAR, *ibid.* **66** (1987) 147-s.
16. D. S. WOOD, P. TERRY and F. J. DICKINSON, in "Development in Pressure Vessel Technology", edited by R. W. Nichols (Applied Science, London, 1980) Vol. 3, p. 145.
17. F. C. HULL, *Welding J.* **46** (1967) 399-s.
18. Y. ARATA, F. MATSUDA and S. KATAYAMA, *Trans. JWRI* **5** (1976) 35.
19. H. ASTROM, B. LOBERG, B. BENGTSSON and K. E. EASTERLING, *Met. Sci.* **10** (1976) 225.

20. V. P. KUNJANPAA, S. A. DAVID and C. L. WHITE, *Welding J* **65** (1986) 203-s.
21. R. C. BERGREN, N. C. COLE, G. M. GOODWIN, J. O. STEGLER, G. M. SLAUGHTER, R. J. GRAY and R. T. KING, *ibid.* **57** (1978) 167-s.
22. S. MATTEAZZI, G. BERNASCONI, G. PIATTI and D. BOERMAN, in Transactions 6th International Conference SMiRT, Paris 1981 (North-Holland, Amsterdam, 1981) Vol. L, paper 12/6.
23. S. MATTEAZZI, G. PIATTI and D. BOERMAN, in Proceedings of the International Conference on Mechanical Behaviour and Nuclear Applications of Stainless Steels at Elevated Temperatures, Varese (Italy) 1981 (The Metals Society, London, 1982) Book 280, p. 194.
24. L. BERTINI, G. PIATTI and E. VITALE, to be presented to ASME Meeting on Constitutive Equation and Life Prediction Models for High Temperature Applications, Berkeley, CA (USA) 1988.
25. S. RAGAZZONI and V. REGIS, ENEL/CRTN Internal Report (Milan, 1982).
26. J. C. LIPPOLD and W. F. SAVAGE, *Welding J.* **58** (1979) 362-s.
27. W. TILLER, K. A. JACKSON, J. W. RUTTER and B. CHALMERS, *Acta Metall.* **1** (1953) 428.
28. G. M. GOODWIN, N. G. COLE and G. M. SLAUGHTER, *Welding J.* **51** (1972) 425-s.
29. T. TAKALO, N. SUUTALA and T. MOISIO, *Metall. Trans. A* **7A** (1976) 1591.
30. N. SUUTALA, T. TAKALO and T. MOISIO, *ibid.* **10A** (1979) 512.
31. N. SUUTALA, T. TAKALO and T. MOISIO, *ibid.* **11A** (1980) 717.
32. S. A. DAVID, *Welding J.* **60** (1981) 63-s.
33. N. SUUTALA, *Metall. Trans. A* **13A** (1982) 2121.
34. J. A. BROOKS, J. C. WILLIAMS and A. W. THOMPSON, *ibid.* **14A** (1983) 23.
35. *Idem., ibid* **14A** (1983) 1271.
36. A. M. RITTER and W. F. SAVAGE, *ibid.* **17A** (1986) 727.
37. O. HAMMAR and U. SVENSSON, in "Solidification and Casting of Metals" (The Metals Society, London 1979) p. 401.
38. W. T. DE LONG, G. A. OSTROM and E. R. SZUMACHOWSKI, *Welding J.* **35** (1956) 562-s.
39. N. SUUTALA, *Metall. Trans. A* **14A** (1983) 191.
40. R. M. BOOTHBY, *Mater. Sci. Technol.* **2** (1968) 78.
41. J. WEGRZYN and A. KLIMPEL, *Welding J.* **60** (1981) 146-s.
42. W. T. DE LONG, *ibid.* **53** (1974) 273-s.
43. C. H. M. JENKINS, E. H. BUCKNALL, C. R. AUSTIN and G. A. MELLOR, *J. Iron Steel. Inst.* **136** (1937) 187.
44. V. R. RIVLIN and G. V. RAYNOR, *Int. Met. Rev.* **1** (1980) 21.
45. J. WEGRZYN and A. KLIMPEL, *Welding J.* **60** (1981) 146-s.
46. P. MARSHALL, "Austenitic Stainless Steels" (Elsevier Applied Science, New York, 1984) p. 117.
47. D. TABOR, *J. Inst. Met.* **79** (1951) 1.

Received 29 February
and accepted 18 July 1988